# Comparison of Permeation Measurements and Hybrid Density-Functional Calculations on Oxygen Vacancy Transport in Complex Perovskite Oxides

D. Gryaznov,*,[†] S. Baumann,[‡] E. A. Kotomin,[†,§] and R. Merkle[§]

[†]Institute for Solid State Physics, University of Latvia, Kengaraga 8, LV-1063 Riga, Latvia

[‡]Forschungszentrum Jülich, Institute of Energy and Climate Research, IEK-1, Materials Synthesis and Processing, 52425 Jülich, Germany

[§]Max Planck Institute for Solid State Research, Heisenbergstr. 1, D-70569 Stuttgart, Germany

Ⓢ *Supporting Information*

ABSTRACT: The oxygen vacancy ($V_O^{\bullet\bullet}$) formation enthalpy (ΔH_F) was determined from the effective activation energies obtained in the permeation measurements on a series of solid solutions $La_{0.98-x}Sr_xCo_{0.2}Fe_{0.8}O_{3-\delta}$ ($x = 0.125-0.8$) and compared with the results of *ab initio* calculations at finite temperatures based on the hybrid (PBE0) and GGA+U calculations, as well as previous thermogravimetric experiments. The Mulliken atomic charges, magnetic moments, and the Fe-$V_O^{\bullet\bullet}$ and Sr-$V_O^{\bullet\bullet}$ distances are analyzed. The strong dependence of formation enthalpy of $V_O^{\bullet\bullet}$ on the Fe oxidation state due to variation in Sr and $V_O^{\bullet\bullet}$ concentrations is discussed.
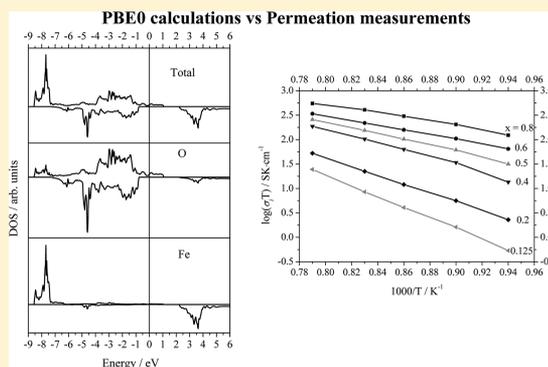
1. INTRODUCTION

(La,Sr)(Co,Fe)O$_{3-\delta}$ (LSCF) is known as one of the best materials for oxygen permeation membranes[1,2] and cathodes in solid oxide fuel cells.[3] This is due to the fact that such complex perovskite oxides show high mixed ionic and electronic conductivities (MIEC) and, hence, high oxygen permeability. The highest oxygen flux is generally observed for dense ceramic membranes having a perovskite structure ABO$_3$ at temperatures above 800 °C (ref 4). This relies on a high concentration of mobile oxygen vacancies as well as a high electronic conductivity. Since the electronic conductivity in perovskites is usually orders of magnitude larger compared to the ionic conductivity, the latter is the limiting transport mechanism, so that permeability (assuming fast surface reaction) can be expressed as

$$j_{O_2} = \frac{RT}{16F^2L}\sigma_i \ln \frac{p'_{O_2}}{p''_{O_2}} \tag{1}$$

where R is the gas constant, T temperature, F Faraday constant, L membrane thickness, σ_i ionic conductivity, and p'_{O_2} and p''_{O_2} the oxygen partial pressure on both sides of the membrane.

High ionic conductivity can be achieved by maximizing diffusivity and particularly concentration of oxygen vacancies. It is well-known that Sr^{2+} ion substituting for La^{3+} is compensated by electronic defects (holes) or oxygen vacancies. The oxygen vacancies prevail over electronic defects at high temperatures.[5]

Such vacancy formation, e.g., in LaFeO$_3$ (LF), can be described (in Kröger–Vink notations[6]) as

$$2SrO \xrightarrow{LaFeO_3} 2Sr'_{La} + V_O^{\bullet\bullet} + 2O_O^x \tag{2}$$

With increasing temperature and/or decreasing oxygen partial pressure, additional vacancies are formed due to partial reduction of the B-site cation, that is, Fe in a solid solution La$_{1-x}$Sr$_x$FeO$_{3-\delta}$ (LSF) decreases its oxidation state from partially 4+ (Fe$_{Fe}^\bullet$) closer to 3+ (Fe$_{Fe}^x$)

$$2Fe_{Fe}^\bullet + O_O^x \rightarrow \frac{1}{2}O_2 + 2Fe_{Fe}^x + V_O^{\bullet\bullet} \tag{3}$$
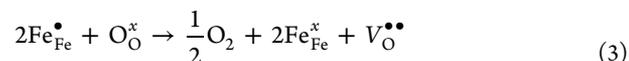
Since Co shows higher reducibility compared to Fe, maximum oxygen fluxes in LSCF can be found for Sr- and Co-rich compounds.[1] On the other hand, excessively high concentration of oxygen vacancies inherently reduces the stability of the crystal lattice, so that pure strontium cobaltite does not have the desired perovskite structure and, hence, permeability vanishes. It turned out that 20 mol % of Fe is sufficient to stabilize the perovskite structure of SrCo$_{0.8}$Fe$_{0.2}$O$_{3-\delta}$ in air. However, in nitrogen atmosphere, i.e., decreased oxygen partial pressure, the perovskite transforms into a brownmillerite phase,[7] which has an ordered arrangement of oxygen vacancies,

resulting again in drastically decreased vacancy mobility. Partial substitution of Sr with Ba helps to avoid the brownmillerite formation in $Ba_{0.5}Sr_{0.5}Co_{0.8}Fe_{0.2}O_{3-\delta}$[7], which shows the highest oxygen fluxes observed so far.[8,9] But still, this compound is close to the stability limits, with regard to crystal structure[10] and reactivity with acid gases. At temperatures below 840 °C an additional hexagonal phase forms reducing oxygen fluxes.[11−13] Moreover, carbonates are easily formed in the presence of CO_2 again drastically reducing the permeability.[14] Therefore, LSCF with limited Sr- and Co-content, although already discovered 30 years ago, has again attracted increasing interest as oxygen transport membrane material; significant oxygen fluxes could be achieved using thin supported membrane layers in $La_{0.6}Sr_{0.4}Co_{0.2}Fe_{0.8}O_{3-\delta}$[2].

The two parent compounds LF and $SrFeO_3$ (SF) are characterized by the existence of Fe ion in the two different oxidation states, Fe^{3+} ($3d^5$) and Fe^{4+} ($3d^4$), respectively. Moreover, LF shows the electronic conductivity increasing with the temperature whereas SF is a metallic compound (at least for small δ). The lattice structure changes from orthorhombic for LF to cubic for SF at room temperature.[15] It would then not be surprising to observe complex magnetic,[16] electrical,[17] and phonon properties[18] for the solid solutions of LF and SF. It is already known from the literature[19] that the $V_O^{\bullet\bullet}$ formation enthalpy for the solid solution LSF changes in a step-wise manner at $\delta = x/2$, where the jump between the oxidation states of Fe (2+/3+ and 3+/4+) occurs.

Recently, we have considered the oxygen vacancy properties in $La_{1-x}Sr_xCo_{0.25}Fe_{0.75}O_{3-\delta}$ using the density functional theory (DFT) for calculating defect formation enthalpy as a function of nonstoichiometry and temperature.[20] The calculated defect formation enthalpy is very close to that from a similar DFT study on LSF due to low content of Co.[21] However, a comparison of the results of these calculations and the thermogravimetric measurements revealed that the calculated formation enthalpy may significantly differ from the measured one at low temperature and high concentrations of Sr although the oxidation entropies suggested no such significant differences. From the experimental point of view, the formation enthalpy may be affected by the oxygen partial pressure and, thus, the Fe oxidation state at fixed Sr content.[19] From the calculation point of view, the magnetic moment on Fe is sensitive to the exchange-correlation functional, affecting the formation enthalpy. It has been shown indeed within the DFT+U calculations and generalized gradient approximation (GGA) by Ritzmann et al.[22] that the inclusion of the strong correlation effects significantly affects the calculated formation energy of $V_O^{\bullet\bullet}$. However, one should keep in mind that the results of such GGA+U calculations depend very much on the choice of Hubbard-U parameter.

The $V_O^{\bullet\bullet}$ migration energy was calculated in LF using the GGA+U approach,[22,23] and in LF, LSF within the standard GGA approach,[24] both studies applied the so-called NEB method as implemented in the VASP code.[25] It was concluded[24] that the defect migration energy is not essentially influenced by the average Sr concentration while the *local* configuration of Sr and/or La in the critical triangle in the saddle point of migration affects the barrier height. Thus, the formation energy of $V_O^{\bullet\bullet}$ and its strong dependence on Sr doping is at the focus of the comparison with the experimental data and represents a key milestone for the DFT calculations. In addition, *hybrid* DFT calculations were shown to be very effective in treatment of the electronic structure of correlated

materials and, in particular, perovskites,[26−29] as well as in calculations of $V_O^{\bullet\bullet}$ formation energy therein.[30] We, therefore, utilize in the present study not only the GGA+U calculations, but also such the hybrid DFT calculations; in order to deeper analyze the defect formation energies in LSF with different Sr concentrations.

Our calculations were motivated by the permeation experiments on the role of Sr doping in oxygen transport. In Section 2 the experimental technique, sample preparation are described. Section 3 is devoted to the computation methods including the computational parameters and calculations of the $V_O^{\bullet\bullet}$ formation energies. Results and Discussion are given in Section 4, subdivided into three subsections: oxygen permeation measurements, the calculated bulk properties and a comparison between the calculated $V_O^{\bullet\bullet}$ properties and experimental results. In Section 5 we present the main conclusions.

2. EXPERIMENTAL SECTION

$La_{0.98-x}Sr_xCo_{0.2}Fe_{0.8}O_{3-\delta}$ ($x = 0.2, 0.4, 0.6, 0.8$) perovskite powders were prepared by spray pyrolysis of the aqueous nitrate solutions containing the corresponding metal nitrates. After spray-drying the powders were calcined at 1200 °C for 5 h and examined by X-ray diffraction (XRD) using a Bruker, D4 Endeavor to ensure phase purity and by inductive coupled plasma−optical emission spectroscopy (ICP-OES) to verify the desired stoichiometry. Lanthanum under-stoichiometry was chosen in order to prevent possible La_2O_3 phases, which lead to sample failure due to high hygroscopy. In case of $x = 0.4$ another powder with stoichiometric La content was prepared, processed, and tested identically. There was no influence of the small La under-stoichiometry on oxygen permeation and, hence, ionic conductivity.

All powders were treated by ball milling in ethanol, using 3 mm ZrO_2 balls, to achieve an average particle size (d_{50}) of 2−4 μm. Samples for oxygen permeation measurements were uniaxially dry pressed and sintered at 1200 °C for 5 h achieving 90% of theoretical density and subsequently ground to an outer diameter of 14.7 mm.

Oxygen permeation measurements of the membranes were conducted in air/Ar gradients with a constant flow rate of 250 mL/min of air as feed gas and 50 mL/min of Ar as sweep gas at varying temperatures. The disc-shaped samples with thickness of 1 mm were sealed with gold rings to the gasket of the quartz glass reactor at 1000 °C. Inner diameter of gold seals is 13 mm leading to 1.33 cm^2 membrane area. The permeated gas was analyzed by a mass spectrometer (Omnistar, Pfeiffer Vacuum).

3. COMPUTATIONAL SECTION

The DFT calculations in the present study are performed using both the plane wave (PW) basis set as implemented in VASP5.2 code[25,31] and the linear combination of atomic orbitals (LCAO) as implemented in CRYSTAL09 code.[32] We will compare the results of DFT+U method[33] and hybrid PBE0[34] exchange-correlation functional (hereafter, functional) important for the proper treatment of the electronic structure of strongly correlated systems such as LSF.[22,35] We give emphasis to the analysis of the electronic density of states (DOS), atomic charges, the z-projection of the magnetic moments (hereafter magnetic moments) on Fe, and the Fe−O bond lengths in perfect as well as defective LSF in the calculations, using both the DFT+U and hybrid PBE0 functionals.

We use, hereafter, the following abbreviations for the two solid solution compositions used in the present study for the analysis of main results in perfect and defective systems: LSF12.5 (12.5% of Sr) for $La_{0.875}Sr_{0.125}FeO_{3-\delta}$ and LSF50 (50% of Sr) for $La_{0.5}Sr_{0.5}FeO_{3-\delta}$.

It is known from XRD measurements[15,16,36] of the crystalline structure of LSF12.5 and LSF50 that the former is orthorhombic at room temperature and rhombohedral at higher temperatures whereas the latter is rhombohedral at low and room temperature but becomes cubic at high temperatures. Thus, for a better comparison of these two compounds we used the rhombohedral symmetry for both LSF12.5 and LSF50.

3.1. Parameters for Density Functional Calculations. In the LCAO calculations, the Gaussian basis set and relativistic pseudopotentials (PPs) of a free La atom with 46 electrons was taken from the PPs library of the Stuttgart/Cologne group.[37] The small-core relativistic effective core pseudopotential replacing 28 electrons and the Gaussian basis set for Sr were taken from ref 38. Notice that the basis set for Sr in our study included the 3d-electron exponent, since in the previous study on $SrTiO_3$[39] this basis set reproduced the phonon properties better than without this exponent. The all-electron basis set 8–411G[40] was used for O atom whereas the all-electron basis set for Fe was taken from ref 41. In order to avoid spurious interactions between the diffuse functions and the core functions of neighboring atoms, the basis set diffuse exponents smaller than 0.15 bohr^{-2} were removed. To optimize the basis set, we used Powell's conjugate-directions minimization method[42] without calculations on the total-energy derivatives as implemented in the basis set optimization code OPTBAS.[43] The bound-constrained optimization was performed for the exponents with 0.1 bohr^{-2} lower bound. The exponents of Gaussian basis functions in noncontracted basis functions were optimized in the calculations with PBE0 functional for rhombohedral LSF50. Notice that this basis set optimization method was already successfully used for $LaCoO_3$[35] and $SrTiO_3$.[39] In Supporting Information (Tables S1–S4) we give the basis set for LSF50 used in the present study.

In the PW calculations we used the projector augmented wave (PAW) method[44] and scalar-relativistic pseudopotentials for 46 electrons on La, 12 electrons on Fe, 28 electrons on Sr, and 2 electrons on O atoms. The exchange-correlation functional was due to Perdew, Burke, and Ernzerhof (PBE).[45] The cutoff energy was fixed at 520 eV throughout all the calculations. The electron occupancies were determined with the Gaussian method using a smearing parameter 0.1 eV. Correspondingly, the rotationally invariant Dudarev's form[46] for the Hubbard correction was used in the PBE+U calculations. However, the advantage of this form is due to the difference $U_{eff} = U - J$, of the Hubbard parameter U and the exchange parameter J. We use, hereafter, the abbreviation PBE+U_{eff} in discussion of the results obtained. We used the two values of U_{eff}, 4.5 and 6.5 eV, to compare not only the bulk properties but also the $V_O^{\bullet\bullet}$ formation enthalpy. A ferromagnetic structure was assumed throughout all the calculations in VASP and CRYSTAL.

In the perovskite-type rhombohedral structure (space group (SG) 167) the primitive unit cell contains 10 atoms, thus, twice the number of atoms in the perovskite-type cubic structure (5 atoms, SG 221).[35] In the present study, we substituted one La atom for one Sr atom in the unit cell containing 10 atoms in order to consider the bulk properties for the content of Sr 50% and to guarantee the highest possible symmetry (SG 155) in

this case. In contrast, the content of Sr 12.5% needs an increase of the unit cell up to 40 atoms, at least, and substituting one La atom for one Sr atom therein. We used the supercell approach[47] for the calculations of LSF12.5 and a single $V_O^{\bullet\bullet}$ in both LSF12.5 and LSF50. The 40 atoms supercell was generated with the help of the transformation matrix $\begin{pmatrix} 2 & 1 & 1 \\ 1 & 2 & 1 \\ 1 & 1 & 2 \end{pmatrix}$ for the translational vectors. A single $V_O^{\bullet\bullet}$ corresponds in such a supercell to the nonstoichiometry $\delta = 0.125$. In addition, the 80 atom supercell (the $2 \times 2 \times 2$ extension of the rhombohedral primitive unit cell) with two Sr ions was used to simulate the case of lower nonstoichiometry, $\delta = 0.0625$ in LSF12.5. In the present study, we used the FINDSYM program of Hatch and Stokes[48] in order to identify the corresponding SG and Wyckoff positions of all atoms in the supercells. Notice that the number of symmetry operations is reduced in CRYSTAL calculations when making the supercells for the non-symmorphic SGs. If the La atom substitutes for the Sr atom in the supercells for LSF12.5, the SG 146 is obtained in the CRYSTAL calculations.

The Monkhorst−Pack scheme[49] for $8 \times 8 \times 8$ k-point mesh in the Brillouin zone was applied to the 10 atoms unit cell, $3 \times 3 \times 3$ to extended 40 atoms and $4 \times 4 \times 4$ to extended 80 atoms supercells. The tolerance factors of 7, 7, 7, 7, and 14 for the Coulomb and exchange integrals calculations were used in the CRYSTAL calculations. Furthermore, the forces for the self-consistent cycles were optimized until the energy difference reached 10^{-7} eV and were smaller than 0.01 eV/Å for the lattice structure optimization (in both perfect and defective crystals) in the CRYSTAL and VASP calculations, respectively.

3.2. Defect Formation Enthalpy. Calculating the enthalpy of $V_O^{\bullet\bullet}$ formation is relevant for a comparison with the results of permeation measurements. The defect formation enthalpy is given by

$$\Delta H_F(T) = E_{tot}^{V_O^{\bullet\bullet}} - E_{tot}^p + \Delta H_{vib}(T) + \frac{1}{2}\mu_{O_2}^0(T) \qquad (4)$$

where superscripts p and $V_O^{\bullet\bullet}$ indicate perfect and defective crystals, E_{tot} total electron energies, and T the temperature. All the energies are given per supercell. The standard chemical potential of oxygen μ_O^0 is given by half the total energy of oxygen molecule plus the vibrational, rotational, and translational contributions, to include the temperature effect. In our previous study[50] we have demonstrated that the calculations of the properties of O_2 with the hybrid PBE0 functional in the LCAO method lead to the very accurate results for the binding energy (5.30 eV), equilibrium distance (1.20 Å), as well as rotational (2.11 K) and vibrational (2478.60 K) temperatures. Therefore, the chemical potential of O_2 in the LCAO calculations reads

$$\mu_{O_2}^0(T) = E_{tot}^{O_2} + E^{O_2} + kT \qquad (5)$$

where $E_{tot}^{O_2}$ the total electronic energy of O_2, E^{O_2} the thermal energy which includes the translational, rotational, and vibrational contributions to the chemical potential of O_2 as calculated within an ideal gas model in the CRYSTAL code, and k Boltzmann's constant. It means that the calculations of ΔH_F with the PBE0 functional in the LCAO method do not need use of any experimental data, in strong contrast to the PW calculations with standard DFT and/or PBE+U_{eff} functionals. We included the vibrational contribution in the solid phase $\Delta H_{vib}(T)$ in the present study by taking data from our previous study on $(La,Sr)Co_{0.25}Fe_{0.75}O_3$,[20] as calculated within the

harmonic approximation and the direct method[51] for calculating phonon frequencies.

As is known, the standard DFT functional in the PW approach leads to errors for the binding energy and/or equilibrium distance of O_2.[52] There are several suggestions in the literature regarding how to correct this effect.[53,54] We rely on the approach suggested by Finnis et al.[55] which is based on the experimental data on oxide heats of formation, thereby avoiding a calculation of the total energy of an oxygen molecule. Thus, the oxygen chemical potential in our PBE+U$_{eff}$ calculations of ΔH_F reads

$$\mu_O^0(T) = E_{tot}^{AO} + \frac{1}{m}E_{vib}^{AO}(T^0) - E_{tot}^A - \frac{1}{l}E_{vib}^A$$
$$- \Delta G^{AO}(T^0) + \Delta H_O(T) \tag{6}$$

where superscripts AO and A stand for the reference binary oxide, and its metal, respectively; in this we have used MgO, T^0 is equal in our case to standard state temperature 298.15 K, ΔG^{AO} is the standard Gibbs free energy of formation, taken from a thermodynamic database,[56] i.e., $\Delta G^{MgO} = 601.6$ kJ/mol. $\Delta H_O(T)$ is the difference in enthalpies at the temperature of interest and standard state, which is also taken from the thermodynamic database.[56] E_{vib} is the vibrational contribution in addition to the internal energy. The prefactors $1/l$ and $1/m$ represent the ratios of the number of atoms in the primitive unit cell to that in the supercell for binary oxide and metal, respectively, which are both $1/27$ for our case.

We used also the so-called *ghost* basis set as implemented in the CRYSTAL code.[32] It assumes that the basis set of a missing O atom remains in the vacancy with a zero core charge. This means that the electron density of two electrons stemming from a missing oxygen atom is divided between the oxygen site and neighboring cations. Thus, use of a ghost basis set provides a reasonable initial guess for the electronic density distribution and in addition allows us to determine the effective electronic charge in the vacancy position.

4. RESULTS AND DISCUSSION

4.1. Oxygen Permeation Measurements. In order to properly compare the results of permeation measurements and present hybrid PBE0 and PBE+U$_{eff}$ calculations, we discuss here the procedure used to deduce the $V_O^{\bullet\bullet}$ formation and migration energy from the experimental profiles. We suppose that the high oxygen permeation in perovskites is due to the conduction mechanism of oxygen ions diffusing through oxygen vacancies in the crystal lattice. According to eq 1, the oxygen permeation rate is proportional to the ionic conductivity at constant thickness, temperature, and oxygen partial pressure gradient.

Normalization of the permeation rate by the geometrical (thickness) and experimental $(\ln(p'_{O_2})/(p''_{O_2}))$ terms results in the *specific permeability*, first introduced by Kharton[57] (assuming fast surface reaction)

$$J_{O_2} = \frac{j_{O_2} \cdot L}{\ln \frac{p'_{O_2}}{p''_{O_2}}} = \frac{R}{16F^2}\sigma_i T \tag{7}$$

According to the Nernst–Einstein-relation, the product of ionic conductivity and temperature is

$$\sigma_i T = \frac{4F^2[V_O^{\bullet\bullet}]D_V}{RV_m} \tag{8}$$

where V_m is the molar volume of the compound, $[V_O^{\bullet\bullet}]$ the oxygen vacancy concentration, and D_V the vacancy diffusion coefficient.

Combining eqs 7 and 8 results in

$$J_{O_2} = \frac{1}{4V_m}[V_O^{\bullet\bullet}]D_V \tag{9}$$

Since the temperature dependence of the molar volume of LSCF is negligible compared to that of $[V_O^{\bullet\bullet}]$ and D_V, the effective activation energy found from the slope of Arrhenius plots of the specific permeability equals a *sum* of the oxygen vacancy formation energy and migration energy (for low $[V_O^{\bullet\bullet}]$, see discussion below).

Figure 1 shows experimental results for a series of solid solutions $La_{0.98-x}Sr_xCo_{0.2}Fe_{0.8}O_{3-\delta}$ with increasing Sr content, x
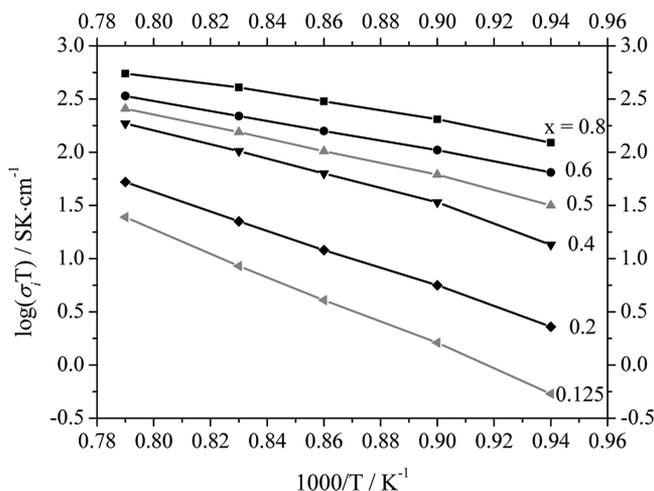
Figure 1. Arrhenius plot of ionic conductivity times temperature of $La_{0.98-x}Sr_xCo_{0.2}Fe_{0.8}O_{3-\delta}$. Black lines represent experimental data for x = 0.2, 0.4, 0.6, and 0.8. Gray lines are interpolated for x = 0.125 and 0.5. Typical error bar is 5%.

= 0.2, 0.4, 0.6, and 0.8. The curves shown are calculated $\sigma_i T$ from oxygen permeation measurements in the temperature range of 1073−1273 K. For $x = 0$ the permeation rate is assumed to be zero due to negligible oxygen vacancy concentration. Using this experimental data set, it is possible to interpolate the specific permeability for each temperature. The resulting lines for x = 0.125 and 0.5 are also plotted in Figure 1. Table 1 shows the respective effective activation

Table 1. $\sigma_i T$@1200 K (in SK/cm) for $La_{0.98-x}Sr_xCo_{0.2}Fe_{0.8}O_{3-\delta}$ and Corresponding Effective Activation Energies E_A (in eV) in the Temperature Range 1073−1273 K According to Figure 1

x	$\sigma_i T$	E_A
0.125	0.89	2.15
0.2	1.35	1.74
0.4	1.93	1.41
0.5	2.15	1.17
0.6	2.29	0.95
0.8	2.60	0.88

energies. We compare the formation enthalpy of $V_O^{\bullet\bullet}$ found from measured effective activation energies by subtracting the corresponding $V_O^{\bullet\bullet}$ migration energies from the DFT calculations:[58] 0.75 and 0.84 eV for LSF12.5 and LSF50, respectively. This leads to a sharp decrease of the predicted $V_O^{\bullet\bullet}$ formation energies as Sr concentration grows: from 1.40 eV down to 0.33 eV.

The equilibrium constant for reaction given by eq 3 depends on temperature via the standard reaction (vacancy formation) enthalpy

$$\ln K = \frac{-\Delta H^0}{RT} + \frac{-\Delta S^0}{R}$$

and is related to the defect concentrations by

$$K = \frac{\sqrt{p_{O_2}}[V_O^{\bullet\bullet}][Fe_{Fe}^x]^2}{[O_O^x][Fe_{Fe}^x]^2}$$

$$= \frac{\sqrt{p_{O_2}}[V_O^{\bullet\bullet}](1 - [Sr_{La}'] + 2\cdot[V_O^{\bullet\bullet}])^2}{(3 - [V_O^{\bullet\bullet}])([Sr_{La}'] - 2\cdot[V_O^{\bullet\bullet}])^2} \quad (10)$$

However, the tempertaure dependence of K does not always directly correspond to the temperature dependence of the vacancy concentration (as extracted from E_a of σ_{ion} in Table 1 and the vacancy migration barrrier). This simple relation holds only for $[V_O^{\bullet\bullet}] \ll [x/2]$ when

$$K \approx \frac{\sqrt{p_{O_2}}[V_O^{\bullet\bullet}](1 - [Sr_{La}'])^2}{3\cdot[Sr_{La}']^2} \propto [V_O^{\bullet\bullet}] \quad (11)$$

On the other hand, for conditions with large $[V_O^{\bullet\bullet}]$ (i.e., high T and/or less positive ΔH^0), the increase of K with increasing temperature (decreasing T^{-1}) mainly corresponds to the term $([Sr'] - 2[V_O^{\bullet\bullet}])$ in the denominator becoming small, while $[V_O^{\bullet\bullet}]$ in the numerator approaches $[Sr']/2$ and is almost constant. Thus, while K increases with decreasing $1/T$, $[V_O^{\bullet\bullet}]$ levels off. In between these two regimes, the slope of σ_{ion} versus $1/T$ gradually decreases. Indeed the curves in Figure 1 indicate some bending, in particular, for materials with high Sr content. Unfortunately, the temperature range covered in the measurement is not large enough to exploit this nonlinearity for fitting the complete defect model (and thus ΔH^0 as defined by eq 11). Nevertheless, one has to keep in mind that ΔH^0 values estimated from Figure 1, assuming validity of the approximate eq 11 might underestimate the real ΔH^0 values.

4.2. Bulk Properties Obtained in Density Functional Calculations. The results of PBE0 and PBE+U_{eff} calculations of bulk properties for LSF50 and LSF12.5 are compared with the experimental data in Tables 2−3. Obviously, the experimental lattice parameters in the rhombohedral LSF50 are better reproduced with the hybrid PBE0 functional than with the PBE+U_{eff} one (Table 2). The latter approach typically overestimates the lattice parameters (if the U_{eff}-parameter is not directly fitted). The calculated lattice parameters for LSF12.5 with PBE0 are close to experiments for the rhombohedral phase (Table 3). Since the substitution of La for Sr in the hypothetical rhombohedral LF with the SG 167 reduces the symmetry of the LSF50 crystal to the SG 155, the oxygen atoms are split and occupy two Wyckoff positions in its 10 atoms unit cell, namely, d for O1 and e for O2. In the 40 atom unit cell of LSF12.5 (SG146) there are 8 oxygen atoms occupying the Wyckoff position b with different coordinates.

Table 2. Calculated Lattice Parameters ($a = b$, c, in Å) Using the Hexagonal Setting, Atomic Charge (q, in e), Magnetic Moment (μ_{Fe} in μ_B) of Fe and the Fe−O Distance in Å in the 10 Atom (Stoichiometric in Oxygen) Unit Cell of LSF50 (SG 155) for PBE0 in the LCAO Calculations and PBE+U_{eff} Functional in the PW Calculations[a]

property		LCAO	PW, PBE+U_{eff}		experiment
		PBE0	U_{eff} = 4.5 eV	U_{eff} = 6.5 eV	
a,b		5.54	5.58	5.59	5.51[b]
c		13.42	13.48	13.49	13.42[b]
q	Sr	1.92	1.58	1.58	
	La	2.65	2.11	2.12	
	Fe	2.24	1.85	1.90	
	O1	−1.50	−1.23	−1.26	
	O2	−1.51	−1.24	−1.27	
μ_{Fe}		4.10	4.06	4.22	3.8[c]
d_{Fe-O}		1.96 [1.97]	1.98 [1.99]	1.98 [2.00]	1.96[c]

[a]See the text for details. Notice that the atomic charge values for the PBE+U_{eff} correspond to the Bader topological analysis[60,61] whereas those for PBE0 are due to the Mulliken population analysis.[62] The values in square brackets correspond to the Fe−O2 distance in LSF50. [b]Ref 59. [c]Neutron diffraction measurements at room temperature for CO/CO_2 quenched samples with high deviation from oxygen stoichiometry.[63]

Table 3. Calculated Lattice Parameters ($a = b$, c, in Å) Using the Hexagonal Setting, Atomic Charge (q, in e), Magnetic Moment (μ_{Fe} in μ_B) of Fe and the Fe−O Distance in Å in the 40 Atom (Stoichiometric in Oxygen) Unit Cell of LSF12.5 (SG 146) for PBE0 in the LCAO Calculations[a]

property		LCAO	experiment
		PBE0	
a,b		5.61	5.61[b]
c		13.46	13.63[b]
q	Sr	1.92	
	La	2.65	
	Fe	2.26	
	O	−1.60	
μ_{Fe}		4.29	
d_{Fe-O}		2.00	1.96−2.00[c]

[a]Due to large number of atoms in the supercell and low symmetry in the CRYSTAL calculations, only the average values for q and μ_{Fe} are given. Notice that the atomic charge values are due to the Mulliken population analysis.[62] [b]Taken from ref 15 at 1023 K. [c]Taken from ref 16 for orthorhombic phase.

Therefore, only the average values for q and μ_{Fe} are given in Table 3. The two split oxygen atoms in LSF50 differ by the distance to Sr and Fe atoms. So, the oxygen atom O1 [O2] has a distance from the Sr atom of 2.55 [2.46] Å in the PBE+U_{eff} calculations, irrespective of the choice of U_{eff} (6.5 or 4.5 eV). The values for the distance between O1[O2] and Sr atoms are slightly larger in the PBE0 calculations, being 2.57 [2.76] Å. It is also seen from the analysis of atomic charges for LSF50 (Tables 2 and 3) that the LCAO calculations with the PBE0 functional suggest a somewhat more ionic picture for LSF50 than the PW calculations with the PBE+U_{eff} functional.

Also, the magnetic moment of Fe (μ_{Fe}) from the PBE0 calculations is slightly larger than that from the PBE+U_{eff} calculations, at least for LSF50 and U_{eff} = 4.5 eV. The d_{Fe-O}-values from PBE+U_{eff} calculations are overestimated, whereas

29546

dx.doi.org/10.1021/jp509206k | J. Phys. Chem. C 2014, 118, 29542−29553
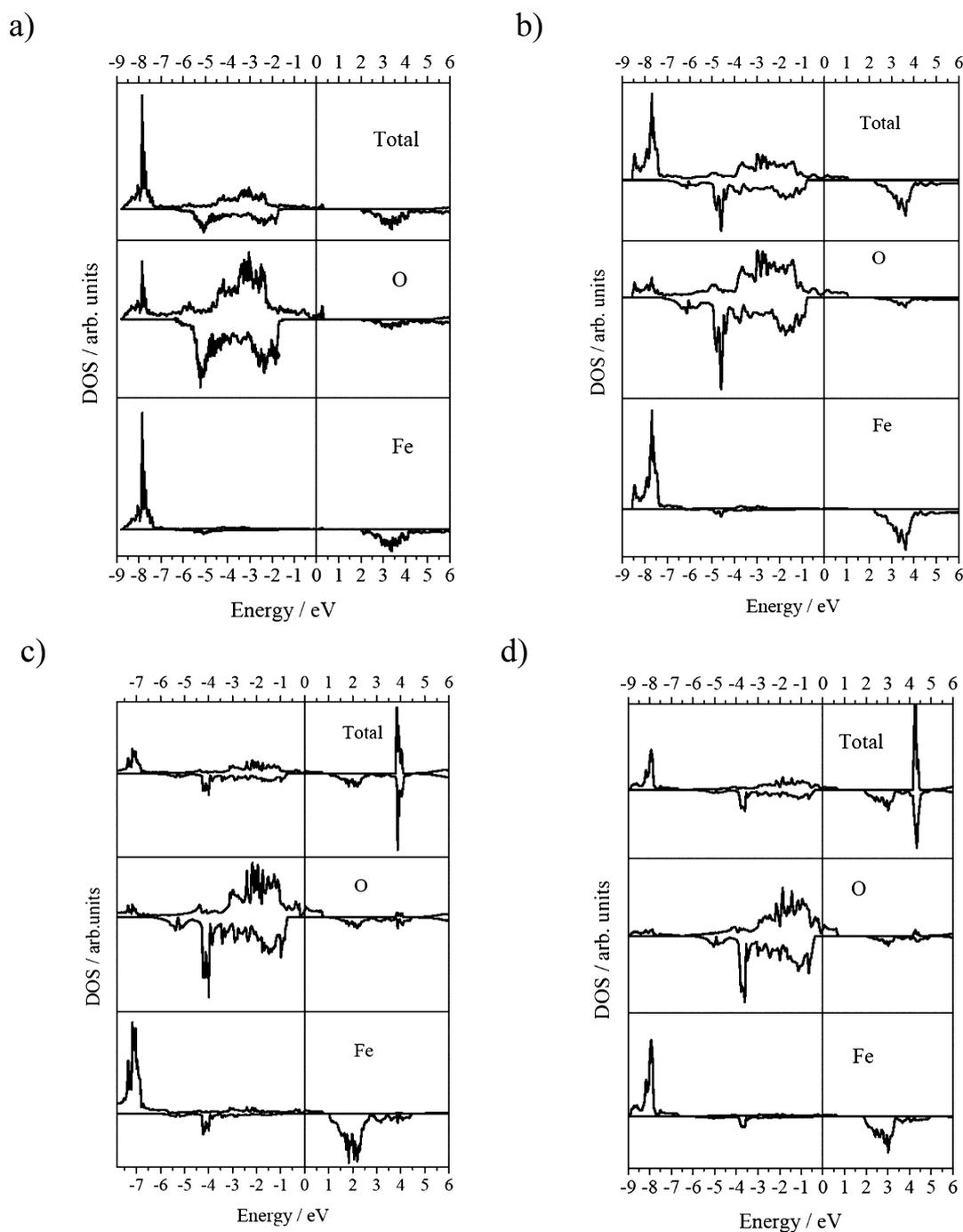
Figure 2. Total and projected density of states (DOS) for stoichiometric in oxygen ($\delta = 0$) LSF12.5 (a) and LSF50 (b), both for the hybrid PBE0 functional, PBE+U$_{\text{eff}}$ functional with U$_{\text{eff}}$= 4.5 eV (c) or U$_{\text{eff}}$ = 6.5 eV (d), all in the FM state. The Fermi energy is taken as zero and indicated by the vertical solid line. The DOS was recalculated with the tetrahedron method in the PBE+U$_{\text{eff}}$ calculations. The DOS for spin-down electrons is represented with negative values.

the PBE0 values are more consistent with the experiments. (A closer comparison of our results and those reported by Ritzmann et al.[22] using the PBE+U$_{\text{eff}}$ approach for LSF50 suggested very similar μ_{Fe} but larger atomic charges for Fe in our case (1.85 e vs 1.70 e) even though very similar values for U$_{\text{eff}}$ (4.5 eV vs 4.3 eV) were applied in both studies. The difference could be attributed to the symmetry of LSF50: rhombohedral in our calculations and cubic in ref 22. As expected, $d_{\text{Fe}-\text{O}}$ is larger in LSF12.5 than in LSF50 which is also confirmed in our PBE0 calculations and previous PBE+U$_{\text{eff}}$ calculations.[22]

We compare below the bulk properties calculated here for LSF with those for LF and use it as a reference material for the analysis of changes in oxidation state of Fe in defective and perfect LSF. The stoichiometric LF was calculated in the LCAO method with the PBE0 functional only. The antiferromagnetic structure and orthorhombic symmetry (SG 62) were assumed. The lattice constants for LF ($a = 5.58$, $b = 5.59$, $c = 7.90$ Å) are in a very good agreement with the experimental values.[17,59] The magnetic moment μ_{Fe} is high (4.28 μ_{B}) in this compound in agreement with the Fe d^5 high spin configuration and the oxidation state of Fe 3+. The moment reduction from

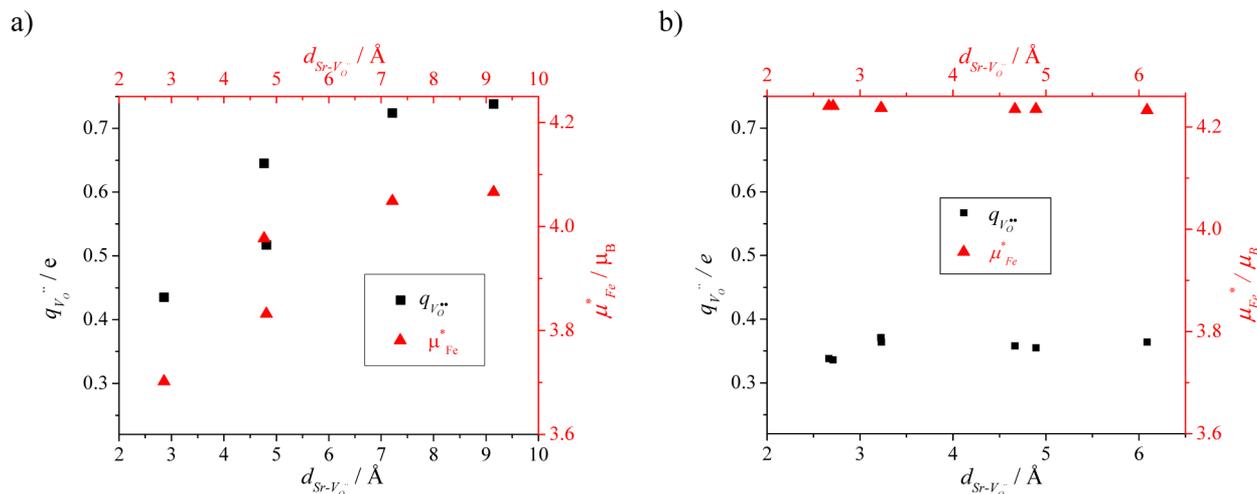**Table 4. Calculated Mulliken Atomic Charge of $V_O^{\bullet\bullet}$ $q_{V_O^{\bullet\bullet}}$ (e) and the Distance between the Fe Ion and $V_O^{\bullet\bullet}$ $d_{Fe-V_O^{\bullet\bullet}}$ (Å) in the LCAO calculations, the Magnetic Moment of Fe Closest to $V_O^{\bullet\bullet}$ μ_{Fe}^* (μ_B), the Enthalpy of $V_O^{\bullet\bullet}$ Formation (eq 4) at 1200 K, ΔH_F (eV), Taking into Account the Temperature Dependence of Oxygen Chemical Potential and Vibrations in the Solid^a**

| | | | DFT | | | | experiments | | |
| | | | | | | | | thermo gravimetry (873−1473 K) | |
x	δ	method/functional	$q_{V_O^{\bullet\bullet}}$	$d_{Fe-V_O^{\bullet\bullet}}$	μ_{Fe}^*	ΔH_F (1200 K)	present ($\delta \leq x/2$)	$\delta \leq x/2$	$\delta > x/2$
12.5	12.5	LCAO/PBE0	0.43	1.77	3.70	2.08	1.40	1.20^b	5.00^b
			0.74	1.91	4.07	2.37			
	6.25	LCAO/PBE0	0.34	2.15	4.24	0.54			
50	12.5		0.36	2.13	4.23	1.09			
		LCAO/PBE0	0.24	2.05	4.24	0.04	0.33	0.99^c	4.12^b
			0.26	2.13	4.23	0.27			
		PW/PBE+U$_{eff}$	-	-	4.18	1.78			
					(4.30)	(1.32)			
			-	-	4.15	1.91			
					(4.29)	(1.44)			

^{a}In the PW PBE+U$_{eff}$ calculations the two values of U_{eff} were used, namely, 4.5 and 6.5 eV. The values of ΔH_F for U_{eff} = 6.5 eV are given in parentheses. Experimental values of ΔH_F are due to the permeation measurements (present study) and the thermogravimetric measurements taken from the literature. The content of Sr x and stoichiometry deviation δ in LSF are given in %. The two values for each property as calculated with the LCAO approach correspond to oxygen vacancies of largest and smallest formation enthalpy ΔH_F. ^{b}Ref 19. ^{c}Measurements for La$_{0.4}$Sr$_{0.6}$FeO$_{3-\delta}$, ref 66.

Figure 3. Mulliken charge of $V_O^{\bullet\bullet}$ and magnetic moment on Fe as functions of $d_{Fe-V_O^{\bullet\bullet}}$ for (a) LSF12.5, (b) LSF50 (both 40 atom supercell, δ = 0.125).

theoretical value of 5 μ_B arises from the covalency effects, which are seen also in the effective atomic charges: q(Fe) = 2.23 e, q(O1) = −1.62 e, q(O2) = −1.63 e.

As is known,[21] the standard GGA functional predicts the LSCF to be formally a metal (the Fermi level crosses the DOS in the valence band). This contradicts the experimental observation that the conductivities of LSF and LSCF increase with the temperature, which is typical for semiconductors.[64] The finite band gap can be better reproduced using either the hybrid PBE0 or PBE+U$_{eff}$ functionals, as also done in the present study. Other approaches may also include the screened hybrid DFT functional which, however, involves the adjustable screening parameter.[26] Figure 2 shows the calculated total and partial density of states (DOS) as obtained with the PBE0 and PBE+U$_{eff}$ functionals. The electron holes are evidenced in the calculated DOS by the presence of O 2p states at the Fermi level, independent of the functional. A strong peak due to the

Fe 3d states (spin-up electrons) is seen in the PBE0 calculations at around −8 eV, followed by the O 2p states for both LSF12.5 and LSF50. Interestingly, there is an admixture of the O 2p states around 8 eV as well in the PBE0 calculations. The same position for this peak of Fe is seen for the PBE+U$_{eff}$ functional with U_{eff} = 6.5 eV. However, the peak is shifted by almost 0.8 eV to smaller energies in the PBE+U$_{eff}$ calculations with U_{eff} = 4.5 eV. The O 2p band (ranging from −6 eV up to the Fermi energy) is characterized by the pronounced (almost separated) peak at −5.8 eV in the spin-down electrons for the PBE0 calculations. Nevertheless, the O 2p band is less hybridized with Fe 3d-states in the PBE+U$_{eff}$ calulations for LSF50. Also, a comparison between the two contents of Sr reveals for LSF50 higher density at the Fermi energy.

4.3. Comparison of Measured and Calculated Oxygen Vacancy Formation Enthalpies. As mentioned above, a single $V_O^{\bullet\bullet}$ was simulated in defective LSF50 and LSF12.5

Figure 4. Mulliken charge of $V_O^{\bullet\bullet}$ and magnetic moment of Fe as functions of $d_{Sr-V_O^{\bullet\bullet}}$ for LSF12.5: (a) $\delta = 0.125$ and (b) $\delta = 0.0625$.

supercells. However, these supercells contain different numbers of nonequivalent oxygen ions occupying different Wyckoff positions. Respectively, as the first step, we identified the Wyckoff positions for O ions in the supercells using the computer code FINDSYM.[48] Second, we calculated the formation enthalpies of all nonequivalent oxygen ions, in order to find those having smallest and largest formation enthalpies at finite temperature. Notice again that the LCAO calculations with the PBE0 functional have an advantage of using the *ghost* basis set in the vacancy position and allow one to estimate the Mulliken charge of $V_O^{\bullet\bullet}$ ($q_{V_O^{\bullet\bullet}}$), the distance of Fe closest to $V_O^{\bullet\bullet}$ ($d_{Fe-V_O^{\bullet\bullet}}$) and its magnetic moment μ_{Fe}^*.

The results of PBE0 and PBE+U_{eff} calculations for $V_O^{\bullet\bullet}$ in LSF12.5 and LSF50 (using both 40 atoms and 80 atom supercells) are presented in Table 4 for the two oxygen vacancies having smallest and largest formation energies, whereas Figure 3 shows the dependence of $q_{V_O^{\bullet\bullet}}$ and μ_{Fe}^* on $d_{Fe-V_O^{\bullet\bullet}}$ for *all* calculated vacancies in the 40 atoms supercells. Also, Figure 4 shows the dependence of $q_{V_O^{\bullet\bullet}}$ and μ_{Fe}^* on $d_{Sr-V_O^{\bullet\bullet}}$ for LSF12.5 with $\delta = 0.125$ and $\delta = 0.0625$.

We have observed that the distances $d_{Fe-V_O^{\bullet\bullet}}$ and $d_{Sr-V_O^{\bullet\bullet}}$ are correlated with $q_{V_O^{\bullet\bullet}}$ and μ_{Fe}^* in LSF12.5 with $\delta = 0.125$: both $q_{V_O^{\bullet\bullet}}$ and μ_{Fe}^* increase considerably with $d_{Fe-V_O^{\bullet\bullet}}$ (Figure 3a) and $d_{Sr-V_O^{\bullet\bullet}}$ (Figure 4a). Thus, the electron population (charge inside vacancy) $q_{V_O^{\bullet\bullet}}$ lies in the region between 0.43 and 0.74 e, as the $d_{Fe-V_O^{\bullet\bullet}}$ distance increases from 1.77 to 1.91 Å and $d_{Sr-V_O^{\bullet\bullet}}$ distance increases from 2.86 to 9.15 Å, respectively (Figures 3a and 4a). The value of μ_{Fe}^* also shows the correlation as discussed: it is smallest (3.70 μ_B) for the shortest $d_{Fe-V_O^{\bullet\bullet}}$ and largest (4.24 μ_B) for the longest $d_{Fe-V_O^{\bullet\bullet}}$ in LSF12.5. That is, there is a considerable dispersion (0.5 μ_B) of magnetic moments in different Fe locations and surroundings in this case of $\delta > x/2$, i.e., involving Fe^{2+} ions.

On the other hand, in the defective supercells of LSF50 with $\delta = 0.125$ and LSF12.5 with $\delta = 0.0625$ the values of parameters $q_{V_O^{\bullet\bullet}}$ and μ_{Fe}^* are less sensitive to the local position of $V_O^{\bullet\bullet}$ within the supercell than in the above-discussed LSF12.5 with $\delta = 0.125$. It is reflected in the small changes of the properties in LSF50 with $\delta = 0.125$ shown in Figure 3b as functions of

$d_{Fe-V_O^{\bullet\bullet}}$. In both the hybrid PBE0 and PBE+U_{eff} calculations for LSF50 with $\delta = 0.125$ and LSF12.5 $\delta = 0.0625$, the total magnetic moment of the supercells increases in the presence of $V_O^{\bullet\bullet}$. Also, its value is independent of the functional. The maximum/minimum values of $q_{V_O^{\bullet\bullet}}$ in LSF50 $\delta = 0.125$ and LSF12.5 with $\delta = 0.0625$ are 0.26/0.24 e (Figure 3b) and 0.34/0.37 e (Figure 4b), respectively, demonstrating more delocalized behavior of electrons left behind by a missing oxygen atom, in comparison with LSF12.5 with $\delta = 0.125$. Interestingly, both LSF50 with $\delta = 0.125$ and LSF12.5 with $\delta = 0.0625$ are characterized by the condition $\delta \leq x/2$.

The distance d_{Fe-O} in defective LSF50 changes in comparison with stoichiometric material, i.e., in such supercells it is not only the Fe ions closest to $V_O^{\bullet\bullet}$ that are affected by the presence of $V_O^{\bullet\bullet}$. For example, the shortest/longest distance d_{Fe-O} in the case of $V_O^{\bullet\bullet}$ having largest formation energy in LSF50 is 1.85/2.00 Å and the Fe magnetic moment is 3.82/4.35 μ_B. Here also the Sr ions play an important role. The closer the Sr ion the longer the distance with Fe., i.e., if $d_{Fe-O} = 1.85/2.00$ Å, then the Sr ion has the distance of 2.68/2.51 Å, respectively.

We present in Table 4 the $V_O^{\bullet\bullet}$ formation enthalpy ΔH_F as given by eq 4 calculated at 1200 K (which is also the temperature closest to the operation temperature of the cathode of the solid oxide fuel cells) for the two functionals used. The calculated values of ΔH_F are compared with those obtained using the results of permeation measurements of the present study and thermogravimetric measurements from the literature. In order to make the comparison at realistic temperatures, the inclusion of vibrational contribution to ΔH_F is necessary. The vibrational contribution in the solid phase ΔH_{vib} was taken from our previous study on (La,Sr)-$Co_{0.25}Fe_{0.75}O_{3-\delta}$.[20] ΔH_{vib} at $T = 1200$ K found with the standard PBE functional in ref 20 for the content of Sr 50% is −0.31 eV for the oxygen nonstoichiometry $\delta = 0.125$. Interestingly, the same contribution for another perovskite ($BaZrO_3$) was obtained using the CRYSTAL code with the PBE0 functional. Notice that the calculated oxidation entropy in ref 20 agrees very well with the measured one.[65] Such calculations of phonon contributions require ground state structure; otherwise, the imaginary frequencies are present and the calculation of free energies is not possible. Because of very time-consuming calculations of phonon vibrations in large supercells, the

estimated value of -0.31 eV was also used for LSF12.5 with $\delta = 0.0625$. The overall contribution of the temperature effects, consisting of the vibrational contribution and kT-term in eqs 4 and 5, is approximately -0.06 eV at 1200 K which is slightly larger than suggested in ref 22 (-0.02 eV at 973.15 K).

According to the defect chemistry model,[19,66] there are two different regimes which should be considered with respect to nonstoichiometry δ and doping x: $\delta \leq x/2$ and $\delta > x/2$. These regimes control the Fe oxidation state, the $V_O^{\bullet\bullet}$ formation energies, and, thus, the oxygen transport in LSF under different conditions. Thus, the formation enthalpy ΔH_F obtained in the thermogravimentric measurements corresponds to different oxidation states: Fe 2+/3+ (large formation enthalpy) and 3+/4+ (low formation enthalpy)[19,66] as were obtained under different experimental conditions controlled by the oxygen partial pressure. The magnitude of ΔH_F corresponding to given oxidation state is nearly a constant, only weakly dependent on dopant concentration x, provided $\delta \leq x/2$. We present in Table 4 the experimental values of ΔH_F extrapolated from the permeation data discussed in Section 4.1 and for $La_{0.9}Sr_{0.1}FeO_{3-\delta}$ and $La_{0.4}Sr_{0.6}FeO_{3-\delta}$ compositions (close to our calculated compositions) taken from the from the thermogravimetry study[19,66] for the above-mentioned two regimes. As mentioned above, the results of permeation measurements demonstrate strong decrease of ΔH_F with Sr doping (1.40 vs 0.33 eV) due to changes of the Fe oxidation state. Our calculations with $\delta = 0.125$ for LSF50 satisfy the criterion $\delta \leq x/2$ whereas $\delta = 0.0625$ for LSF12.5 lies at the border between the two Fe oxidation states (2+/3+ and 3+/4+, i.e., $\delta = x/2$).

The calculated values of ΔH_F given in Table 4 for two extreme vacancy configurations for LSF50 with $\delta = 0.125$ (the average oxidation state 3.25) as obtained in the PBE0 calculations lie in the range 0.04–0.27 eV (the average value 0.16 eV), in reasonable agreement with the permeation measurements ($\Delta H_F = 0.33$ eV) but smaller than in the thermogravimetry experiments (0.99 eV). On the other hand, the defect formation enthalpy $\Delta H_F = 0.54$–1.09 eV (the average value 0.83 eV) for LSF12.5 with $\delta = 0.0625$ (average oxidation state is 3.0) in the PBE0 calculations reasonably agrees not only with the value of 1.40 eV from the permeation measurements, but also with 1.20 eV from the thermogravimetry measurements. Thus, our calculations reproduce the general trend of a moderate decrease of the $V_O^{\bullet\bullet}$ formation energy with the Sr concentration increase (and vice versa). In contrast, the opposite regime $\delta > x/2$ for LSF12.5 with $\delta = 0.125$ (average oxidation state is 2.875) is characterized by the average calculated value of $\Delta H_F = 2.07$ eV, which is more than by 1 eV larger in a comparison with the above-discussed $\delta = x/2$. This results from the presence of 12.5% of Fe^{2+} in this compound and high energy price for their formation from Fe^{3+}. Note that the calculated average value of 2.07 eV should be compared with the average of experimental energies of 1.2 and 5.0 eV (Table 4), i.e., 3.1 eV since a sequential release of the two electrons from the oxygen vacancy occurs in the two stages, with $0 \leq \delta \leq x/2$ and $x/2 < \delta$.

In Figure 5 we also present the variation in ΔH_F as a function of $d_{Sr-V_O^{\bullet\bullet}}$ for LSF12.5 with $\delta = 0.0625$. It is worth mentioning that the variation in ΔH_F is larger for LSF12.5 with $\delta = 0.0625$ (where $V_O^{\bullet\bullet}$ can be very close to or far from Sr) than LSF50 with $\delta = 0.125$ (where $V_O^{\bullet\bullet}$ will always be close to Sr), cf., the low variations in the formation energy of $V_O^{\bullet\bullet}$ in ref 21.
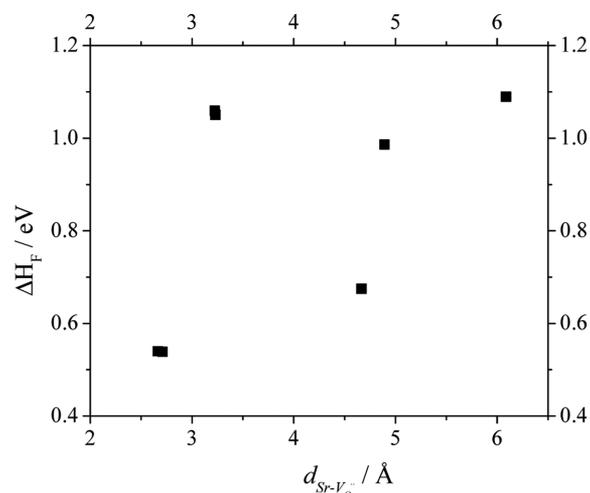

Figure 5. Formation enthalpy of $V_O^{\bullet\bullet}$ (ΔH_F at 1200 K) as a function of $d_{Sr-V_O^{\bullet\bullet}}$ for LSF12.5 with $\delta = 0.0625$. The chosen values of ΔH_F correspond to $q_{V_O^{\bullet\bullet}}$—and μ_{Fe}^*-values in Figure 4b.

The analysis of Fe magnetic moments in Table 4 shows that in the oxidation state Fe 3+ (LSF12.5, $\delta = 0.0625$) they are closest to those in pure LF (4.28 μ_B,) with the same oxidation state, whereas for other compounds the magnetic moments are reduced, due to increased fraction of Fe^{4+} or Fe^{2+} (both having 4 unpaired spins but different configurations: d^4 and d^6, respectively).

Note that the absolute values of ΔH_F in the PBE+U_{eff} calculations (Table 4) differ considerably from the results of permeation measurements, and the hybrid PBE0 calculations. This brings us the conclusion that the hybrid PBE0 functional provides us with the most accurate description of bulk LSF and $V_O^{\bullet\bullet}$ behavior therein.[67]

5. CONCLUSIONS

The DFT calculations based on the hybrid PBE0 functional (with the standard exact exchange contribution of 25%) and the LCAO basis set were combined with the permeation measurements to analyze the formation enthalpy of oxygen vacancies in complex perovskites like $(La,Sr)FeO_{3-\delta}$ with different Sr doping. The use of hybrid functionals allows us to reproduce the bulk properties of these solid solutions and their behavior as semiconductors. The finite band gap is important to calculate properly the formation enthalpy of $V_O^{\bullet\bullet}$ in LSF which is in agreement with previous experimental studies on the formation enthalpy of $V_O^{\bullet\bullet}$ in LSF. Moreover, the LCAO basis set allowed us to determine the electronic densities within the vacancy (due to additional so-called ghost basis set at the vacancy site) and find the correlation between the charge of $V_O^{\bullet\bullet}$, the Fe-$V_O^{\bullet\bullet}$ distance, and the magnetic moment on Fe. It is demonstrated that a careful comparison of the calculation results with the experiments requires the knowledge of the oxidation state of Fe under experimental conditions and thus the relation between nonstoichiometry δ and doping x. We have confirmed that the formation enthalpy of $V_O^{\bullet\bullet}$ significantly decreases with the Sr doping, which greatly accelerates oxygen transport through permeation membranes and SOFC cathodes.

ASSOCIATED CONTENT

Ⓢ Supporting Information

Exponents (bohr^{-2}) and contraction coefficients. This material is available free of charge via the Internet at http://pubs.acs.org.

AUTHOR INFORMATION

Corresponding Author

*E-mail: gryaznov@mail.com. Mailing address: Institute of Solid State Physics, University of Latvia, Kengaraga 8, Riga, LV-1063, Latvia. Phone: +371-67187480.

Notes

The authors declare no competing financial interest.

ACKNOWLEDGMENTS

REFERENCES

(1) Teraoka, Y.; Zhang, H. M.; Okamoto, K.; Yamazoe, N. Mixed ionic-electronic conductivity of $La_{1-x}Sr_xCo_{1-y}Fe_yO_3$ perovskite-type oxides. *Mater. Res. Bull.* **1988**, 23 (1), 51−58.

(2) Serra, J. M.; Garcia-Fayos, J.; Baumann, S.; Schulze-Küppers, F.; Meulenberg, W. A. Oxygen permeation through tape-cast asymmetric all-$La_{0.6}Sr_{0.4}Co_{0.2}Fe_{0.8}O_{3-\delta}$ membranes. *J. Membr. Sci.* **2013**, 447, 297−305.

(3) Serra, J. M.; Uhlenbruck, S.; Meulenberg, W. A.; Buchkremer, H. P.; Stöver, D. Non-structuring of solid oxide fuel cells. *Top. Catal.* **2006**, 40 (1−4), 123−131.

(4) Sunarso, J.; Baumann, S.; Serra, J. M.; Meulenberg, W. S.; Liu, S.; Lin, Y. S.; Diniz da Costa, J. C. Mixed Ionic-Electronic Conducting (MIEC) Ceramic-Based Membranes for Oxygen Separation. *J. Membr. Sci.* **2008**, 320, 13−41.

(5) Bouwmeester, H. J. M.; Den Otter, M. W.; Boukamp, B. A. Oxygen transport in $La_{0.6}Sr_{0.4}Co_{1-y}Fe_yO_{3-\delta}$. *J. Solid State Electrochem.* **2004**, 8, 599−605.

(6) Kröger, F. A.; Vink, H. J. Relations between the Concentrations of Imperfections in Crystalline Solids. *Solid State Physics* **1956**, 3, 307−435.

(7) McIntosh, S.; Vente, J. F.; Haije, W. G.; Blank, D. H. A.; Bouwmeester, H. J. M. Structure and Oxygen Stoichiometry of $SrCo_{0.8}Fe_{0.2}O_{3-\delta}$ and $Ba_{0.5}Sr_{0.5}Co_{0.8}Fe_{0.2}O_{3-\delta}$. *Solid State Ionics* **2006**, 177, 1737−1742.

(8) Shao, Z.; Yang, W.; Cong, Y.; Dong, H.; Tong, J.; Xiong, G. Investigation of the Permeation Behavior and Stability of a $Ba_{0.5}Sr_{0.5}Co_{0.8}Fe_{0.2}O_{3-\delta}$ Oxygen Membrane. *J. Membr. Sci.* **2000**, 172 (1−2), 177−188.

(9) Baumann, S.; Serra, J. M.; Lobera, M. P.; Escolástico, S.; Schulze-Küppers, F.; Meulenberg, W. A. Ultrahigh Oxygen Permeation Flux through Supported $Ba_{0.5}Sr_{0.5}Co_{0.8}Fe_{0.2}O_{3-\delta}$ Membranes. *J. Membr. Sci.* **2011**, 377, 198−205.

(10) Kuklja, M. M.; Mastrikov, Yu. A.; Jansang, B.; Kotomin, E. A. The Intrinsic Defects, Disordering, and Structural Stability of $Ba_xSr_{1-x}Co_yFe_{1-y}O_{3-\delta}$. *J. Phys. Chem. C* **2012**, 116, 18605−18611.

(11) Švarcová, S.; Wiik, K.; Tolchard, J.; Bouwmeester, H. J. M.; Grande, T. Structural Instability of Cubic Perovskite $Ba_xSr_{1-x}Co_{1-y}Fe_yO_{3-\delta}$. *Solid State Ionics* **2008**, 178, 1787−1791.

(12) Niedrig, C.; Taufall, S.; Burriel, M.; Menesklou, W.; Wagner, S. F.; Baumann, S.; Ivers-Tiffée, E. Thermal Stability of the Cubic Phase in $Ba_{0.5}Sr_{0.5}Co_{0.8}Fe_{0.2}O_3$ (BSCF) 1. *Solid State Ionics* **2011**, 197, 25−31.

(13) Arnold, M.; Wang, H.; Martynczuk, J.; Feldhoff, A. In situ Study of the Reaction Sequence in the Sol-Gel Synthesis of a $(Ba_{0.5}Sr_{0.5})(Co_{0.2}Fe_{0.8})O_{3-\delta}$ Perovskite by X-ray Diffraction and Transmission Electron Microscopy. *J. Am. Ceram. Soc.* **2007**, 90 (11), 3651−3655.

(14) Arnold, M.; Wang, H.; Feldhoff, A. Influence of CO_2 on the Oxygen Permeation Performance and the Microstructure of Perovskite-Type $(Ba_{0.5}Sr_{0.5})(Co_{0.2}Fe_{0.8})O_{3-\delta}$ Membranes. *J. Membr. Sci.* **2007**, 293, 44−52.

(15) Fossdal, A.; Menon, M.; Wærnhus, I.; Wiik, K.; Einarsrud, M.-A.; Grande, T. Crystal Structure and Thermal Expansion of $La_{1-x}Sr_xFeO_{3-\delta}$ Materials. *J. Am. Ceram. Soc.* **2004**, 87 (10), 1952−1958.

(16) Dann, S. E.; Currie, D. B.; Weller, M. T.; Thomas, M. F.; Al-Rawwas, A. D. The Effect of Oxygen Stoichiometry on Phase Relations and Structure in the System $La_{1-x}Sr_xFeO_{3-\delta}$ ($0 \leq x \leq 1, 0 \leq \delta \leq 0.5$). *J. Solid State Chem.* **1994**, 109, 134−144.

(17) Mizusaki, J.; Sasamoto, T.; Cannon, W. R.; Bowen, H. K. Electronic Conductivity, Seebeck Coefficient, and Defect Structure of $La_{1-x}Sr_xFeO_3$ (x = 0.1, 0.25). *J. Am. Ceram. Soc.* **1983**, 66 (4), 247−252.

(18) Tajima, S.; Masaki, A.; Uchida, S.; Matsuura, T.; Fueki, K.; Sugai, S. Infrared Reflectivity and Electronic States in Perovskite-Type Oxides $La_{1-x}Sr_xFeO_3$ and $La_{1-x}Sr_xCoO_3$. *J. Phys. C: Solid State Phys.* **1987**, 20, 3469−3484.

(19) Mizusaki, J.; Yoshihiro, M.; Yamauchi, S.; Fueki, K. Thermodynamic Quantities and Defect Equilibrium in the Perovskite-Type Oxide Solid Solutions $La_{1-x}Sr_xFeO_{3-\delta}$. *J. Solid State Chem.* **1987**, 67, 1−8.

(20) Gryaznov, D.; Finnis, M. W.; Evarestov, R. A.; Maier, J. Oxygen Vacancy Formation Energies in Sr-Doped Complex Perovskites: *ab Initio* Thermodynamic Study. *Solid State Ionics* **2014**, 254, 11−16.

(21) Kuklja, M. M.; Kotomin, E. A.; Merkle, R.; Mastrikov, Yu. A.; Maier, J. Combined Theoretical and Experimental Analysis of Processes Determining Cathode Performance in Solid Oxide Fuel Cells. *Phys. Chem. Chem. Phys.* **2013**, 15, 5443−5471.

(22) Ritzmann, A. M.; Muñoz-García, A. B.; Pavone, M.; Keith, J. A.; Carter, E. A. Ab Initio DFT+U Analysis of Oxygen Vacancy Formation and Migration in $La_{1-x}Sr_xFeO_{3-\delta}$ (x=0, 0.25, 0.50). *Chem. Mater.* **2013**, 25, 3011−3019.

(23) Ritzmann, A. M.; Muñoz-García, A. B.; Pavone, M.; Keith, J. A.; Carter, E. A. Ab Initio Evaluation of Oxygen Diffusivity in $LaFeO_3$: the Role of Lanthanum Vacancies. *MRS Commun.* **2013**, 1, 1−6.

(24) Mastrikov, Y. A.; Merkle, R.; Kotomin, E. A.; Kuklja, M. M.; Maier, J. Formation and Migration of Oxygen Vacancies in $La_{1-x}Sr_xCo_{1-y}Fe_yO_3$ Perovskites: Insight from Ab Initio Calculations and Comparison with $Ba_{1-x}Sr_xCo_{1-y}Fe_yO_{3-\delta}$. *Phys. Chem. Chem. Phys.* **2013**, 15, 911−918.

(25) Kresse, G.; Furthmüller, J. *VASP the Guide*; University of Vienna: Vienna, 2013.

(26) Franchini, C. Hybrid Functional Applied to Perovskites. *J. Phys.: Condens. Matter.* **2014**, 26, 253202.

(27) Zhukovskii, Yu. F.; Kotomin, E. A.; Evarestov, R. A.; Ellis, D. E. Periodic Models in Quantum Chemical Simulations of F Centres in Crystalline Metal Oxides. *Int. J. Quantum Chem.* **2007**, 107, 2956.

(28) Evarestov, R. A.; Kotomin, E. A.; Mastrikov, Yu. A.; Gryaznov, D.; Heifets, E.; Maier, J. Comparative Density Functional LCAO and Plane Wave Calculations of $LaMnO_3$ Surfaces. *Phys. Rev. B* **2005**, 72, 214411.

(29) Eglitis, R. I.; Piskunov, S.; Heifets, E.; Kotomin, E. A.; Borstel, G. Ab Initio Study of the $SrTiO_3$, $BaTiO_3$ and $PbTiO_3$ (001) Surfaces. *Ceramic International* **2004**, 30, 1989−1992.

(30) Alexandrov, V. E.; Kotomin, E. A.; Maier, J.; Evarestov, R. A. First-Principles Study of Bulk and Surface Oxygen Vacancies in $SrTiO_3$. *Eur. Phys. J. B* **2009**, 72, 53−57.

(31) Kresse, G.; Furthmüller, J. Efficiency of ab-Initio Total Energy Calculations for Metals and Semiconductors Using a Plane-Wave Basis Set. *Comput. Mater. Sci.* **1996**, 6, 15−50.

(32) Dovesi, R.; Saunders, V. R.; Roetti, C.; Orlando, R.; Zicovich-Wilson, C. M.; Pascale, F.; Civalleri, B.; Doll, K.; Harrison, N. M.; Bush, I. J.; D'Arco, Ph.; Llunell, M. *CRYSTAL-09 User's Manual*; University of Turin: Turin, 2010.

(33) Anisimov, V. I.; Solovyev, V. I.; Korotin, M. A.; Czyżyk, M. T.; Sawatzky, G. A. Density-Functional Theory and NiO Photoemission Spectra. *Phys. Rev. B* **1993**, *48* (23), 16929−16934.

(34) Perdew, J. O.; Ernzerhof, M.; Burke, K. Rationale for Mixing Exact Exchange with Density Functional Approximations. *J. Chem. Phys.* **1996**, *105*, 9982−9985.

(35) Gryaznov, D.; Evarestov, R. A.; Maier, J. Hybrid Density-Functional Calculations of Phonon in LaCoO₃. *Phys. Rev. B* **2010**, *82*, 224301.

(36) Braun, A.; Richter, J.; Harvey, A. S.; Erat, S.; Infortuna, A.; Frei, A.; Pomjakushina, A.; Mun, B. S.; Holtappels, P.; Vogt, U.; Conder, K.; Gauckler, L. J.; Graule, T. Electron Hole-Phonon Interaction, Correlation of Structure, and Conductivity in Single Crystal La₀.₉Sr₀.₁FeO₃₋δ. *Appl. Phys. Lett.* **2008**, *93*, 262103.

(37) Available online at: http://www.theochem.uni-stuttgart.de/pseudopotentials/clickpse.html.

(38) LaJohn, L. A.; Christiansen, P. A.; Ross, R. B.; Atashroo, T.; Ermler, W. C. Ab Initio Relativistic Effective Potentials with Spin-Orbit Operators. III. Rb through Xe. *J. Chem. Phys.* **1987**, *87* (5), 2812−2824.

(39) Evarestov, R. A.; Blokhin, E.; Gryaznov, D.; Kotomin, E. A.; Maier, J. Phonon Calculations in Cubic and Tetragonal Phases of SrTiO₃: A Comparative LCAO and Plane Wave Study. *Phys. Rev. B* **2011**, *83*, 134108.

(40) Bredow, T.; Jug, K.; Evarestov, R. A. Electronic and Magnetic Structure of ScMnO3. *Phys. Status Solidi B* **2006**, *243*, R10−R12.

(41) Catti, M.; Valerio, G.; Dovesi, R. Theoretical Study of Electronic, Magnetic, And Structural Properties of α-Fe₂O₃ (hematite). *Phys. Rev. B* **1995**, *51*, 7441−7450.

(42) Press, W. H.; Teukolski, S. A.; Vetterling, V. T.; Flannery, B. P. *Numerical Recipes in FORTRAN 77: The Art of Scientific Computing*; Press Syndicate of the University of Cambridge: New York, 2001.

(43) Evarestov, R. A.; Panin, A. I.; Bandura, A. V.; Losev, M. V. Electronic Structure of Crystalline Uranium Nitrides UN, U₂N₃ and UN₂: LCAO calculations with the Basis Set Optimization. *J. Phys.: Conf. Series* **2008**, *117*, 012015.

(44) Kresse, G.; Joubert, D. From Ultrasoft Pseudopotentials to the Projector Augmented-Wave Method. *Phys. Rev. B* **1999**, *59* (3), 1758−1775.

(45) Perdew, J. P.; Burke, K.; Ernzerhof, M. Generalized Gradient Approximation Made Simple. *Phys. Rev. Lett.* **1996**, *77*, 3865−3868.

(46) Dudarev, S. L.; Nguyen Manh, D.; Sutton, A. P. Effect of Mott-Hubbard Correlations on the Electronic Structure and Structural Stability of Uranium Dioxide. *Philos. Mag. B* **1997**, *75*, 613−628.

(47) Evarestov, R. A. *Quantum Chemistry of Solids*; Springer: Heidelberg, 2013.

(48) Stokes, H. T.; Hatch, D. M. *FINDSYM*: Program for Indentifying the Space-Group Symmetry of a Crystal. *J. Appl. Crystallogr.* **2005**, *38*, 237−238 http://stokes.byu.edu/iso/findsym.php.

(49) Monkhorst, J.; Pack, J. D. Special Points for Brillouin-Zone Integrations. *Phys. Rev. B* **1976**, *13*, 5188−5192.

(50) Gryaznov, D.; Blokhin, E.; Sorokine, A.; Kotomin, E. A.; Evarestov, R. A.; Bussmann-Holder, A.; Maier, J. A Comparative *Ab Initio* Thermodynamic Study of Oxygen Vacancies in ZnO and SrTiO₃: Emphasis on phonon contribution. *J. Phys. Chem. C* **2013**, *117*, 13776−13784.

(51) Grimvall, G. *Thermophysical properties of Materials*; North-Holland: Amsterdam, 1986.

(52) Bocharov, D.; Gryaznov, D.; Zhukovskii, Yu. F.; Kotomin, E. A. *Ab Initio* Modeling of Oxygen Impurity Atom Incorporation into Uranium Mononitride Surface and Sub-Surface Vacancies. *J. Nucl. Mater.* **2011**, *416*, 200−204.

(53) Wang, L.; Maxisch, Th.; Ceder, G. Oxidation Energies of Transition Metal Oxides within the GGA+U Framework. *Phys. Rev. B* **2006**, *73*, 195107.

(54) Lee, Y.-L.; Kleis, J.; Rossmeisl, J.; Morgan, D. *Ab Initio* Energetics of LaBO₃(001) (*B*=Mn, Fe, Co, and Ni) for Solid Oxide Fuel Cell Cathodes. *Phys. Rev. B* **2009**, *80*, 224101.

(55) Finnis, M. W.; Lozovoi, A. Y.; Alavi, A. The Oxidation of NiAl: What Can We Learn from *Ab Initio* Calculations. *Annu. Rev. Mater. Res.* **2005**, *35*, 167−207.

(56) NIST, *NIST Chemistry Webbook*; NIST, 2010; http://webbook.nist.gov/chemistry/.

(57) Kharton, V. V.; Viskup, A. V.; Yaremchenko, A. A.; Kerko, P. F.; Naumovich, E. N.; Kovalevsky, A. V. Ionic Transport in SrCo₀.₈₅Ti₀.₁₅O₃₋δ. *Mater. Res. Bull.* **1999**, *34* (12−13), 1921−1928.

(58) The climbing image nudged elastic band method as implemented in VASP was used to find the oxygen migration barrier in La₀.₈₇₅Sr₀.₁₂₅Co₀.₂₅Fe₀.₇₅O₂.₈₇₅ and La₀.₅Sr₀.₅Co₀.₂₅Fe₀.₇₅O₂.₈₇₅ for better comparison of the experimental and calculation results in the present study. Special care was undertaken to ensure a consistent treatment of the lattice distortion pattern, extending through the whole supercell, for both initial and transition states of O migration to avoid artifact contributions of the structural distortion to the migration barrier. The supercells as those discussed in ref 20 for La₀.₈₇₅Sr₀.₁₂₅Co₀.₂₅Fe₀.₇₅O₂.₈₇₅ and La₀.₅Sr₀.₅Co₀.₂₅Fe₀.₇₅O₂.₈₇₅ were used for these calculations on the migration barrier. In such supercells different atomic arrangements were tried to find those which are most energetically favorable and can then be used for identifying the migration barrier. It was found, in accordance with the literature,[23] that the migration barrier is independent of the Sr content.

(59) Haas, O.; Vogt, U. F.; Soltmann, C.; Braun, A.; Yoon, W.-S.; Yang, X. Q.; Graule, T. The Fe K-edge X-ray Absorption Characteristics of La₁₋ₓSrₓFeO₃₋δ Prepared by Solid State Reaction. *Mater. Res. Bull.* **2009**, *44*, 1397−1404.

(60) Bader, R. *Atoms in Molecules: A Quantum Theory*; Oxford University Press: New York, 1990.

(61) Henkelman, G.; Arnaldsson, A.; Jónsson, H. A Fast and Robust Algorithm for Bader Decomposition of Charge Density. *Comput. Mater. Sci.* **2006**, *36*, 354−360.

(62) Mulliken, R. S. Electronic Population Analysis on LCAO-MO Molecular Wave Functions. I. *J. Chem. Phys.* **1955**, *23* (10), 1833−1840.

(63) Yang, J. B.; Yelon, W. B.; James, W. J.; Zhou, X. D.; Xie, Y. X.; Anderson, H. U. Magnetic and Mössbauer Studies on Oxygen Deficient Perovskite, La₀.₆Sr₀.₄FeO₃₋δ. *J. Appl. Phys.* **2002**, *91*, 7718−7720.

(64) Tai, L.-W.; Nasrallah, M. M.; Anderson, H. U.; Sparlin, D. M.; Sehlin, S. R. Structure and Electrical Properties of La₁₋ₓSrₓCo₁₋ᵧFeᵧO₃. Part 2. The System La₁₋ₓSrₓCo₀.₂Fe₀.₈O₃. *Solid State Ionics* **1995**, *76*, 273−283.

(65) Bucher, E.; Sitte, W.; Caraman, G. B.; Cherepanov, V. A.; Aksenova, T.; Ananyev, M. V. Defect Equilibria and Partial Molar Properties of (La,Sr)(Co,Fe)O₃. *Solid State Ionics* **2006**, *177*, 3109−3115.

(66) Mizusaki, J.; Yoshihiro, M.; Yamauchi, S.; Fueki, K. Nonstoichiometry and Defect Structure of the Perovskite-Type Oxides La₁₋ₓSrₓFeO₃₋δ. *J. Solid State Chem.* **1985**, *58*, 257−266.

(67) Our average value of 0.16 eV for the formation enthalpy at 1200 K for LSF50 is by 0.17 eV larger than the average ΔH_F = −0.01 eV at 973.15 K in ref 22 demonstrating, on one hand, the same trends in the behavior of ΔH_F in both studies but, on the other hand, better agreement of LCAO PBE0 results with the experiments. It was also mentioned[22] that there is an error in ΔH_F of at least 0.42 eV due to overbinding of O₂ in the standard DFT calculations. In our study we found that this error might be much larger. The two effects can explain differences in the PBE+U$_{eff}$ results for ΔH_F between the present study and the one in ref 22. We calculated ΔH_F at 0 K using the PBE+U$_{eff}$ approach and fixing the volume of the "pseudocubic" 40 atoms unit cell with the FM configuration during the calculation of $V_O^{\bullet\bullet}$ in the supercell. Furthermore, the total energy of O₂ was taken from the

standard DFT calculation. ΔH_F in this case is reduced significantly (in comparison with data in Table 4), varying in the range from 0.38 to 1.07 eV at U_{eff} = 4.5 eV.

29553

dx.doi.org/10.1021/jp509206k | *J. Phys. Chem. C* 2014, 118, 29542−29553